Measurement Science
and Technology

Enhanced grating characterization method for absorbing X-ray gratings by bidirectional angular X-ray transmission

To cite this article before publication: Constantin Rauch *et al* 2025 *Meas. Sci. Technol.* in press https://doi.org/10.1088/1361-6501/adde7c

Enhanced grating characterization method for absorbing X-ray gratings by bidirectional angular X-ray transmission

Constantin Rauch[1]‡, Stephan Schreiner[1], Pascal Meyer[2], Veronika Ludwig[1], Markus Schneider[1], Christopher Sowinski[1], Gisela Anton[1], Thilo Michel[1], Stefan Funk[1]

[1] Erlangen Centre for Astroparticle Physics, Nikolaus-Fiebiger-Str. 2, 91058 Erlangen, Germany
[2] Karlsruhe Institute of Technology, Institute of Microstructure Technology, Hermann-von-Helmholtz-Platz 1, 76344 Eggenstein-Leopoldshafen, Germany

E-mail: constantin.rauch@fau.de

February 2025

Abstract. High-quality X-ray absorption gratings are essential for grating-based X-ray phase-contrast imaging. Bidirectional angular X-ray transmission measurements, as proposed in this work, allow for large-area and nondestructive characterization of these gratings.

A custom setup consisting of two rotational axes is used to measure the transmission of X-ray absorption gratings under rotation. From the transmission values and rotation angles, pixelwise transmission profiles are reconstructed. From these transmission profiles, parameter maps that carry information about the microstructure of the grating are retrieved via a fitting procedure. Compared to unidirectional angular X-ray transmission measurements, more detailed and complementary parameter maps are obtained, revealing more defects and parameter variations. Apart from duty cycle, absorber height, and absorber inclination, the bidirectional measurements also provide access to grating lamella rotation on the substrate and to auxiliary structures introduced to increase grating stability.

Furthermore, a novel correction technique is introduced to address projective distortions in individual radiographs caused by the rotations. This method relies on calibration phantom measurements to track the movement of registration points under the same rotations as the gratings. Based on the movement of the registration points, the distortions are reconstructed, and appropriate deformation vector fields are calculated and applied to measurement data, achieving a correction with a precision of about two pixels.

Keywords: X-ray imaging, X-ray absorption gratings, X-ray interferometers

‡ Corresponding author.

1. Introduction

Grating-based X-ray phase-contrast imaging emerged as a promising enhancement to conventional absorption-based imaging methods. In addition to the standard attenuation image, a differential phase image and a dark-field image are obtained using this technique. These image modalities have proven valuable in various fields; for example, medical imaging, see [1, 2], nondestructive testing [3], and high-energy-density physics [4].

For grating-based phase-contrast imaging, a set consisting of two or three gratings is required [5]. At least one of these gratings is typically an absorption grating, meaning a grating consisting of a high-Z material, such as gold, with sufficiently high structures to absorb all X-rays impinging on the bars (about 200 µm for 50 keV [6]). The periods required for grating-based phase-contrast are in the micrometer range (typically 1 µm to 25 µm), therefore the aspect ratio, which is given by the ratio of grating absorber height to grating bar width, is high. This poses a challenge for production processes and impacts longevity of the gratings, especially since the grating quality plays a crucial role in obtaining high-quality imaging results [4]. Furthermore, some grating parameters, such as absorber height, can only be defined indirectly during grating manufacturing, necessitating rigorous parameter measurements.

Measuring microstructures, of which X-ray absorption gratings are an example, remains a challenging undertaking. Optical and stylus-based profilometry methods are constantly improved to increase sensitivity and measurement area [7, 8]. Nonetheless, only comparatively small areas can be probed and the high aspect ratios of X-ray gratings limit profilometry methods to the surface of the grating structure.

Measurements of periodic surface microstructures are possible using scattering-based methods at different photon wavelengths. These methods have recently been optimized for probing optical diffraction gratings [9, 10], and the requirements for modeling the structures under test to obtain meaningful results have been reduced [11, 12]. However, scatterometry also probes only the surface and is not suitable for obtaining information about the high-aspect-ratio absorbing structures of X-ray gratings.

Alternatively, scanning electron microscopy (SEM) is available as a tool for quality control in grating manufacturing. To preserve the stability of the structure, the stabilizing resist is typically left intact. The grating is sputtered with approximately 10 nm of Au or Ag, and the resist structure is measured. In this way, the grating period and the duty cycle (see subsection 2.1) are measured, and surface defects and cracks can be identified. Measuring absorber height with SEM is possible but requires destruction of the gratings. Furthermore, although recent developments have enabled faster imaging and larger fields of view [13], SEM remains limited to only probing small areas of the gratings.

In [14], the authors proposed angular X-ray transmission (AXT) measurements to achieve large-scale characterization of absorption gratings with medical or laboratory-

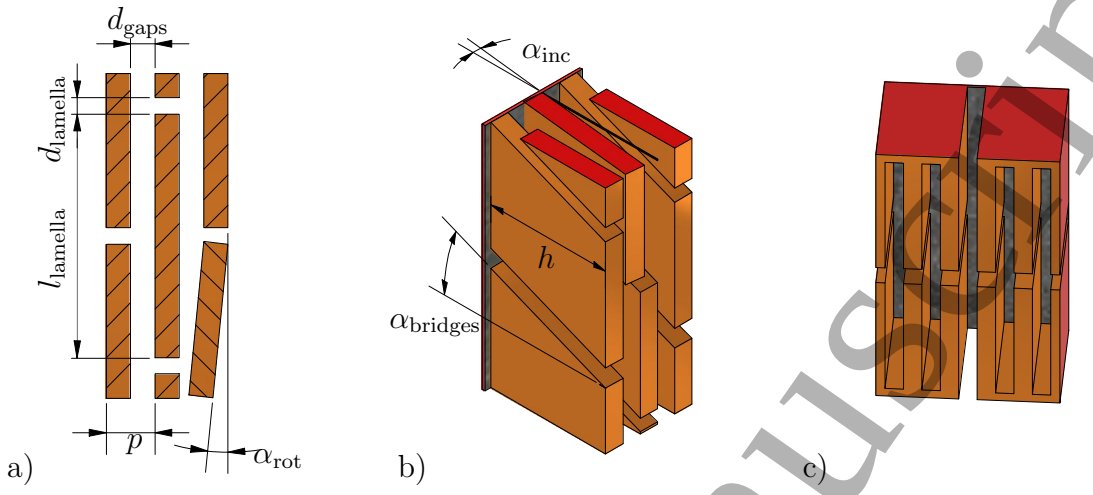

Figure 1: Sketches of grating structures for gratings manufactured using deep X-ray lithography. Structures drawn in orange are absorbing structures, the grating substrate is shown in gray. Cut edges drawn in red indicate that the structure continues in that direction. a) depicts the frontal projection of a standard layout grating, b) a tilted view onto the side of the grating lamellae. c) shows two halves of a unit cell of an inverted layout grating with the large cross shaped grating gap in the center. The deviations shown in the sketches typically stretch over multiple lamellae in real gratings, which is omitted here for clarity. Sketches are not drawn to scale.

grade X-ray sources and detectors. AXT measurements enable the retrieval of absorber height, duty cycle (i.e., the ratio between grating bars and grating period), and absorber inclination from a series of radiographs acquired under varying rotational angles of the grating at cone beam sources. However, the method as presented in [14] neglects the two-dimensional nature of real absorption gratings.

Here, we propose extending AXT measurements to take effects stemming from the two-dimensional characteristics of gratings into account. This is achieved by rotating the grating around two axes instead of one during data acquisition. Additionally, a novel method for correcting projection distortions that are caused by the rotation of the grating is introduced. These enhancements significantly improve the quantity and quality of information obtained from the measurements.

2. Methods

2.1. X-ray absorption gratings

Various manufacturing techniques for producing X-ray absorption gratings exist, see for example [15] and [16]. This work focuses on gratings manufactured with deep X-ray lithography ([17, 18]) in a process called “LIGA” (German acronym for lithography,

galvanization, and molding), as these gratings are available to the authors. The new method is suitable for gratings produced with other techniques, such as deep reactive ion etching [19] as well, provided that the grating structure is similar to the one produced by "LIGA".

In "LIGA", a wafer, made for example from silicon or graphite, is coated with photoresist. Using coherent synchrotron radiation and a lithography mask, the structure of the grating is imprinted into the full depth of the photoresist. The resist is then developed, and the exposed areas are removed chemically. The resulting voids are filled by electroplating, thereby growing the grating bars.

The standard layout of a grating structure created in this way is shown from two different perspectives in Figure 1 a) and b). In these gratings, the grating bars are divided into multiple grating lamellae with a lamella length l_{lamella}, separated by resist bridges of length d_{lamella}. These bridges increase grating structure stability. Since recently, these bridges can be manufactured at an angle $\alpha_{\mathrm{bridges}}$ relative to the grating normal to reduce unwanted X-ray transmission. The fill factor (FF) is defined in the following as the ratio of grating bar filled with absorbing material, compared to resist bridge length. It can be calculated via

$$\mathrm{FF} = \frac{l_{\mathrm{lamella}}}{l_{\mathrm{lamella}} + d_{\mathrm{lamella}}}. \tag{1}$$

A larger fill factor means that the grating structure is closer to the ideal grating structure, possibly resulting in overall better interferometer performance.

The total area A in a grating unit cell is one grating period in one direction and one lamella period perpendicular. The ratio of grating area that is covered with absorbing material $A_{\mathrm{absorbing}}$ in a unit cell, compared to the total area, is called area duty cycle

$$\mathrm{DC}_A = \frac{A_{\mathrm{absorbing}}}{A} \tag{2}$$

in the following. It is influenced by the one-dimensional design duty cycle DC defined as the ratio of the grating period p that is covered with absorbing structures:

$$\mathrm{DC} = 1 - \frac{d_{\mathrm{gaps}}}{p}, \tag{3}$$

where d_{gaps} is the width of the gap between grating bars.

The absorber height h is chosen based on the planned set-up X-ray energy to ensure sufficient absorption. It is set during the galvanization step. In addition, the absorbing structures may be inclined at an angle α_{inc} relative to the grating substrate either intentionally ([20] and [21]) or as a result of grating structure collapse. This is illustrated in Figure 1 b) for one of the lamellae.

The lamellae may also be rotated on the grating substrate compared to the perfect vertical alignment by a rotation angle α_{rot} as indicated in Figure 1 a). This may occur locally due to shifts within the substrate or globally due to wafer alignment.

"LIGA" can also be used to produce other grating layouts, an example of a different layout called "inverted layout" is shown in Figure 1 c). It is similar to a structure obtained by switching the areas in a standard layout grating, replacing

those areas filled with resist with ones filled with absorbing material, and vice versa. The interconnected lamellae and long vertical and horizontal resist bridges increase grating structure stability at the cost of larger deviation from the ideal grating layout transmission profile.

2.2. Two-dimensional angular X-ray transmission

Angular X-ray transmission measurements, first introduced in [22] and [14], are based on changes in the projected height profiles of grating structures described in subsection 2.1, as gratings are rotated. These variations in effective height are quantified by monitoring changes in X-ray transmission during grating rotation about an axis parallel to the lamella direction within the grating plane, referred to as the φ-axis in the following.

The 1D AXT measurements are extended using a second rotation axis, in the following called θ-axis, which is perpendicular to the φ-axis and also lies in the grating substrate plane. With this second axis, effects stemming from the 2D grating layout are detectable. A transmission surface acquired by a rotation around both axes is presented as an example in Figure 2. The transmission of multiple grating periods needs to be averaged for such an AXT surface to form; therefore, multiple periods must be captured within a single pixel. This is not a restriction when using common flat panel X-ray detectors with resolutions worse than typical grating structure sizes.

A global peak Ⓐ is present near the origin of the coordinate system in Figure 2. At this peak, the X-rays impinge perpendicular on the grating substrate, aligning parallel to the absorber walls. As a result, transmission reaches its maximum, as the projection of the non-absorbing areas, comprising the regions between the lamellae and the bridge area, are at their largest.

Moving in positive or negative θ direction, the transmission slightly decreases, forming a ridge denoted by Ⓑ in Figure 2. This reduction is due to the resist bridges being increasingly shadowed as the tilt in θ direction grows. Moving in positive or negative φ direction (the standard AXT measurements), the transmission decreases rapidly. At specific angles,

$$\varphi_{\min} = \arctan\left(n\frac{p}{h}\right), \quad n \in \mathbb{N} \tag{4}$$

local transmission minima are observed [14]. For $\theta \approx 0$, no local minima are detected for most gratings. The absence of these minima is attributed to the resist bridges, as the increased transmission caused by the bridges obscures the expected minima. By moving away from the $\theta = 0$ axis in the positive or negative θ direction, the bridges are shadowed, avoiding this effect. This reveals the four minima symmetrically surrounding the global peak. One such minimum is marked as point Ⓒ in Figure 2.

2.3. Projection- and cone beam correction

The θ and φ rotations of the grating in front of the detector introduce distortions between radiographs acquired at different angles. Two effects, identified in [14], contribute to

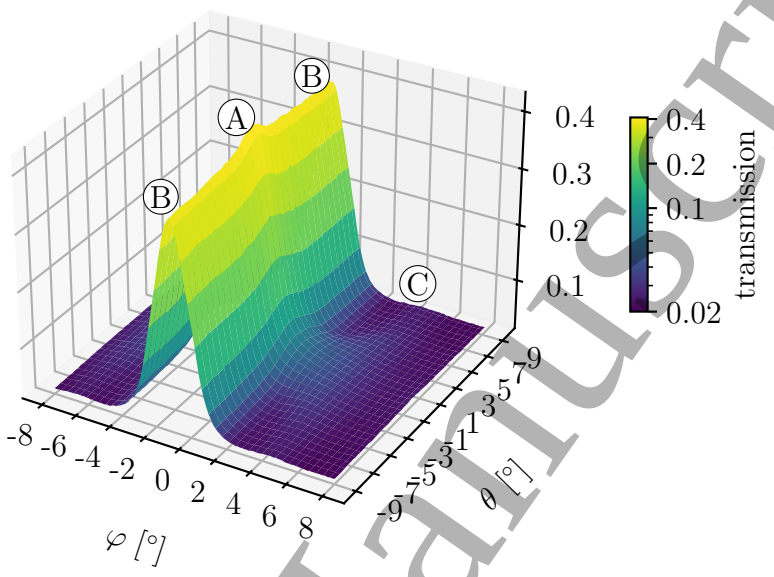

Figure 2: 2D transmission profile of a standard-layout grating with 6 µm period and 80 µm design height. The graph shows the transmission values measured in a pixel behind the grating on the z-axis and in logarithmic color code. The φ-axis is an axis of rotation parallel to the grating bars. The θ-axis is oriented perpendicular within the grating plane. Circled letters indicate the regions of interest: Ⓐ shows the global maximum, Ⓑ denotes the ridges and Ⓒ points at one of the four local minima surrounding the global maximum.

these distortions: First, the rotations shift detector coordinates corresponding to the same grating points. Second, if a diverging beam is used, the impingement angle of the X-rays additionally varies over the grating area and with rotation. These distortions are transferred to the retrieved parameter maps unless these effects are corrected.

Figure 3 illustrates the setup geometry required to determine and correct the distortions. The projection of a point at G in the grating coordinate system onto a point G′ in the detector plane is given by the intersection of a ray passing through the grating point with the detector plane. Assuming the X-rays originate from the global coordinate origin $O\,(0,0,0)$, and with D the distance between source and detector, the intersection is calculated via

$$\begin{aligned} \vec{X} \quad &= t \cdot \vec{x}_{\mathrm{G,\,global}},\ t = \frac{D}{\left(\vec{x}_{\mathrm{G,\,global}}\right)_{\mathrm{z}}}, \quad \text{with} \\ \vec{x}_{\mathrm{G,\,global}} &= R_{\theta,\varphi}\left(R_{\mathrm{G}}\,\vec{x}_{\mathrm{G}}\right) + T_{\mathrm{rot}}, \end{aligned} \tag{5}$$

using the vectors $\vec{X}$, $\vec{x}_{\mathrm{G,\,global}}$ pointing at G′ and G in the global system, and $\vec{x}_{\mathrm{G}}$ pointing at G in the grating system, as shown in Figure 3 b). T_{rot} represents the translations from

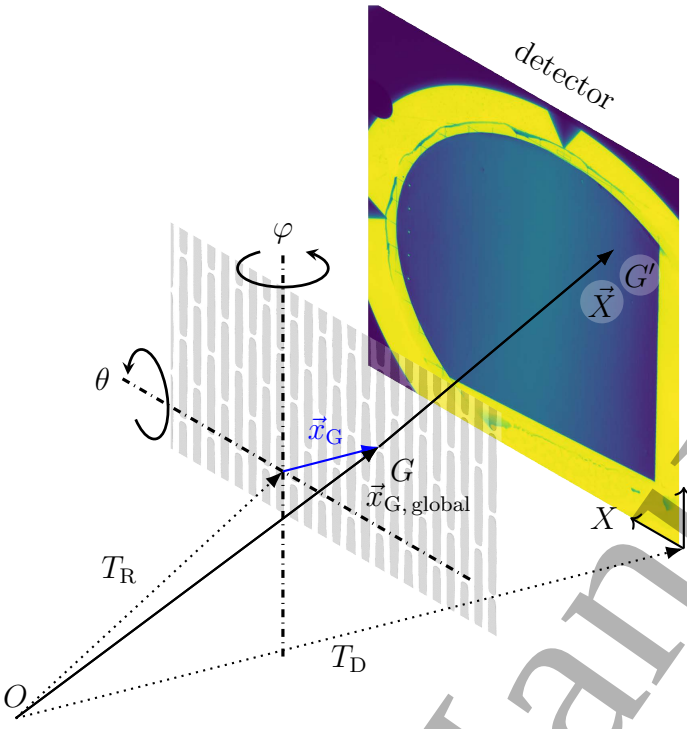

Figure 3: Sketch of the setup geometry. Three coordinate systems are used: The global system with the X-ray source at its origin O, the grating system reached via translation T_{R} and rotation $R_{\varphi,\theta}$ and the detector system onto which grating points are projected, shifted by T_{D} from the origin. Vectors are marked with solid arrows, coordinate transforms with dashed arrows and rotational axes with double dashed lines. Shown within the detector is a typical radiograph obtained during AXT measurements.

the rotated coordinates to the global system. R_{G} accounts for a possible grating rotation around its normal, which could occur due to non-optimal mounting of the grating. $R_{\theta,\varphi}$ models the rotation performed for the AXT measurement in θ and φ direction.

Correcting the distortions based solely on the measured setup geometry is challenging due to the large number of parameters in Equation 5 that would need to be measured with high precision, particularly at high magnifications. To address this, we propose an alternative approach.

The movement of a set of test points is tracked by acquiring radiographs of a high-contrast calibration phantom in a separate measurement. This information allows all points in each radiograph to be mapped back to their corresponding points on the grating, enabling precise calculation of transformations between image coordinates at different AXT angles. To this end, the registration points found in each radiograph are used to fit D, T_{Rot} and R_{G} in Equation 5 to a model of the registration points. For the fit, the Euclidean distances between the model point positions projected onto the detector plane and the measured registration point positions are minimized using nonlinear least-squares optimization. The fitting process compensates for uncertainties in the measurements, which would otherwise arise when determining the required

Table 1: Overview of grating parameters and their definitions from grating geometry. Parameters with definition "direct" are explicitly indicated in Figure 1, others are composites of multiple geometric parameters. Also listed are the features in the AXT surface (see Figure 2), from which the grating parameters are retrieved.

Parameter name	Symbol	Definition	Retrieval from
duty cycle	DC	$1 - d_{\text{gaps}}/p$	ridge transmission maximum
area duty cycle	DC_A	$A_{\text{absorbing}}/A$	global transmission maximum
fill factor	FF	$l_{\text{lamella}}/\left(l_{\text{lamella}} + d_{\text{lamella}}\right)$	DC and DC_A
absorber height	h	direct	φ of first minima
absorber inclination	α_{inc}	direct	φ of ridge maxima
resist bridge tilt	α_{bridges}	direct	θ of global maximum
lamella rotation	α_{rot}	direct	θ and φ of ridge maxima

transformations purely from geometric considerations. Transformations obtained with this method can be used for multiple AXT measurements, provided that the setup geometry is identical between calibration and measurement.

Two of the grating parameter retrievals discussed in the following section—absorber inclination α_{inc} and resist bridge tilt α_{bridges}—depend on the absolute angles at which certain features are measured. An additional gradient is introduced into these parameter maps by varying X-ray impingement angles caused by cone beam sources. For gratings examined in this manuscript, which are manufactured with upright absorbers, the average gradient is determined using a linear fit over the entire grating area and then subtracted from the map to remove the gradient.

2.4. Grating parameter retrieval

A framework was developed in Python and C++ that performs the aforementioned corrections and extracts the relevant information from the 2D AXT transmission surfaces through data fitting. The following sections describe the process of obtaining the grating parameters outlined in subsection 2.1. Table 1 provides an overview of the grating parameters and their relationship to the grating structure, AXT surface, and each other.

Duty cycle: For sufficiently high absorbing structures or sufficiently low photon energies, the transmission through the absorbing structures approaches zero. This means that X-rays are only transmitted through the parts of the grating where no absorbing material is present. In an ideal 1D grating with continuous grating bars, the average transmission over a grating area is therefore a good measure for the duty cycle [14]. If resist bridges are present within the grating, the average intensity behind the grating increases due to transmission through these resist bridges.

Within the 2D transmission surface, the duty cycle information is available where the angle θ is large enough such that the resist bridges are shadowed and do not

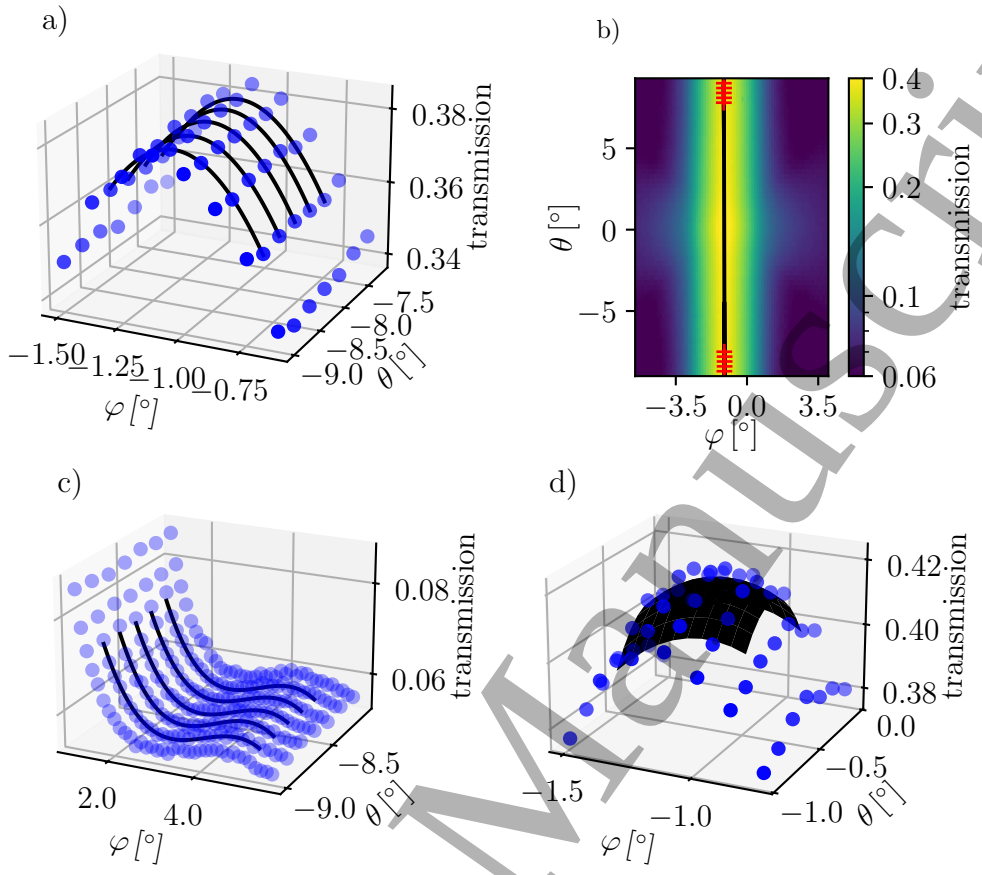

Figure 4: Fits to the AXT surface for extracting grating parameters. Solid black lines indicate the fits, blue circles denote measured AXT data points. a) shows five fits to one of the ridge regions Ⓑ in Figure 2. b) shows the linear fit to the ridge positions (red markers) as determined from the fit in a) plotted over the transmission of the ridge. Presented in c) are five valley Ⓒ fits. d) shows a 2D fit (black surface) for determining the position and height of the global maximum Ⓐ.

contribute to the transmission through the grating. This occurs at the ridges in the AXT surfaces (Ⓑ in Figure 2), and the duty cycle is given by

$$\mathrm{DC} = 1 - I_{\mathrm{ridge}}, \tag{6}$$

where I_{ridge} represents the normalized transmission measured at the ridges. The angular distance of the ridges from the global maximum depends on the width of the resist bridges and the absorber height, as larger resist bridges mean a larger angle θ is necessary to fully shadow the bridges.

The framework performs multiple fits perpendicular to the ridge to extract the height. The fit width, number of fits, and the θ distance from the global maximum are configurable parameters. The fit can be conducted either using a parabolic function or, as proposed in [14], a triangular function. The results obtained from these multiple fits are averaged to obtain a single ridge transmission value, which is then used to calculate

the duty cycle according to Equation 6. Example fits to a ridge are shown in Figure 4 a).

Absorption within the grating substrate can significantly reduce transmission through the grating. The extent of this reduction depends on factors such as the substrate material, its thickness, and the acceleration voltage used during measurement. To estimate and correct for absorption by the wafer, the transmission through a region containing only the substrate is measured.

Absorber inclination: Inclined absorbing structures shift the position of transmission maxima to different locations along the φ-axis [14]. The locally averaged inclination can be obtained from the same fits required for the duty cycle determination by identifying the $\varphi_{\max}$ coordinate of the maximum of each fit. Angled illumination caused by the cone beam of X-ray tubes introduces a gradient into the absorber inclination map, which requires correction as described in subsection 2.3.

Structure rotation: A new parameter map obtainable with the 2D AXT measurement reveals the rotation of lamella structures on top of the grating substrate plane, α_{rot}. This map is particularly sensitive to deviations in the orientation of grating lamellae and global rotations of the absorbing structure. Simulations indicate that a rotation of the grating around the beam axis causes the entire 2D AXT surface to rotate around the central peak.

The rotation of the ridge relative to the $\varphi = 0$ axis is quantified by performing a linear fit to the previously determined ridge maximum positions $\varphi_{\max,\,i}$ and $\theta_{\max,\,i}$:

$$\theta_{\max,\,i} = m \cdot \varphi_{\max,\,i} + t \tag{7}$$

Such a fit is presented in Figure 4 b). The angle is then calculated from the slope (m) of the fit function as

$$\alpha_{\mathrm{rot}} = \arctan\left(m\right). \tag{8}$$

Absorber height: As described in [14], the absorber height is obtained from AXT surfaces via the transmission minima that result from the projected height profile becoming uniform at the angle

$$\alpha_{\min} = \arctan\left(\frac{p}{h}\right). \tag{9}$$

The positions of several minima per quadrant of the transmission surface are determined by cubic fits to the relevant regions. See Figure 4 c) for an example of the cubic fits. From the fit function, the local minimum $\alpha_{\min}$ is retrieved, and by solving Equation 9 for h, the absorber height map is obtained.

If only 1D AXT measurements are performed, and the grating is not oriented vertically, the angular positions of the first minima are determined with an error, as only the distance along the φ direction is measured. With 2D AXT measurements, the rotation of the grating is detectable and its effect on the absorber height measurements can be compensated for.

Area duty cycle and fill factor: The area duty cycle can be determined directly from the maximum transmission value $I_{\max}$ of the transmission surface as

$$\mathrm{DC}_A = 1 - I_{\max}. \tag{10}$$

The framework extracts the maximum transmission by applying a 2D polynomial fit to a small area surrounding the global maximum of the transmission surface. An example of this fit is presented in Figure 4 d).

The fill factor is conceptually similar to the duty cycle. However, the prominence of minima in AXT curves decreases for lower duty cycles ([14]), and the dominant contribution to the transmission surface stems from the grating gaps. Hence, no minimum along the ridge of the transmission surface in θ direction will be present for the vast majority of gratings. Instead, the fill factor can also be calculated from the duty cycle and the area duty cycle via

$$\mathrm{FF} = \frac{\mathrm{DC}_A}{\mathrm{DC}}. \tag{11}$$

The framework first determines the area duty cycle and then calculates the fill factor according to Equation 11.

Resist bridge tilt: Maximum global transmission is reached when X-rays can propagate through both the resist bridges and the grating gaps. Retrieving the angle θ of the maximum transmission allows finding the angle of the resist bridge walls relative to the grating normal.

The framework extracts the angle θ of the maximum from the 2D-fit to the global maximum of the transmission surface. Similar to the absorber inclination, cone beam correction is required for the resist bridge tilt in order to correct for the inclined illumination of the grating surface.

3. Experiment and Results

The data was acquired using a Comet high-power tungsten X-ray tube operated at 45 kV and 45 mA in combination with a Teledyne DALSA Shad-o-Box 6k HS flat panel detector with a pixel pitch of 49.5 µm and a field of view of 14.5 cm by 11.4 cm. Dark frame subtraction and flat field correction are applied to detector images before further processing. All measurements were taken with a source-to-sample distance of 1.4 m and a sample-to-detector distance of 18.5 cm.

A custom measurement apparatus consisting of two high-precision rotary stages (Physik Instrumente PRS 200, Standa 8MR151) and a grating mounting jig was specifically designed to ensure reproducible movement of the gratings under test. A CAD sketch of the apparatus is shown in Figure 5. The placement of the rotary stages in the setup ensures that the two rotational axes intersect within the grating substrate.

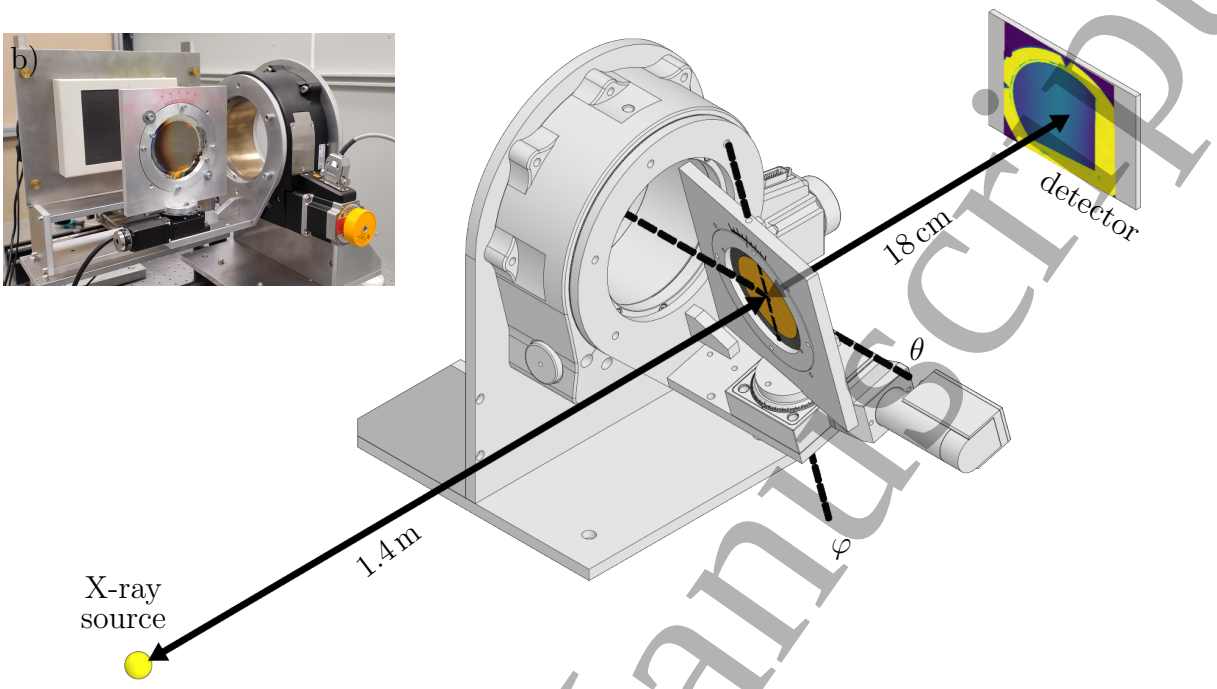

Figure 5: Setup used for AXT measurements. The setup consists of an X-ray source, a custom measurement apparatus with two rotary stages, and a detector. The grating under test (circular gold surface) is mounted to the custom apparatus. The inset b) shows an image of the grating, rotary stages and detector.

3.1. Projective correction

The projective correction is performed using a calibration phantom consisting of a nine-by-nine grid of holes with a diameter of 1 mm centered on a 10 cm diameter round disk. A design sketch is presented in Figure 6 a). This dimension matches the majority of grating formats available to the authors. The design is manufactured from a copper plate with 0.5 mm thickness. The high contrast produced by copper allows for a reduction of acquisition times for phantom images by an order of magnitude compared to regular AXT radiographs. A radiograph and the registration points found by the analysis framework using a 2D peak finding algorithm are shown in Figure 6 b).

The registration points are then used in the fit described in subsection 2.3 to obtain the transformations between the radiographs. Sensible starting values are provided, and parameter constraints are imposed to ensure high-quality fit results. As a benchmark of the applied model, Figure 6 c) shows deviations of the fitted hole positions from the positions determined by the peak finding algorithm for a center image, where the X-rays impinge onto the grating perpendicular in the central beam, and an image where the grating is rotated by 7° in θ direction and 8° in φ direction. The deviation between fitted registration points and measured positions is in the order of two pixels, for many

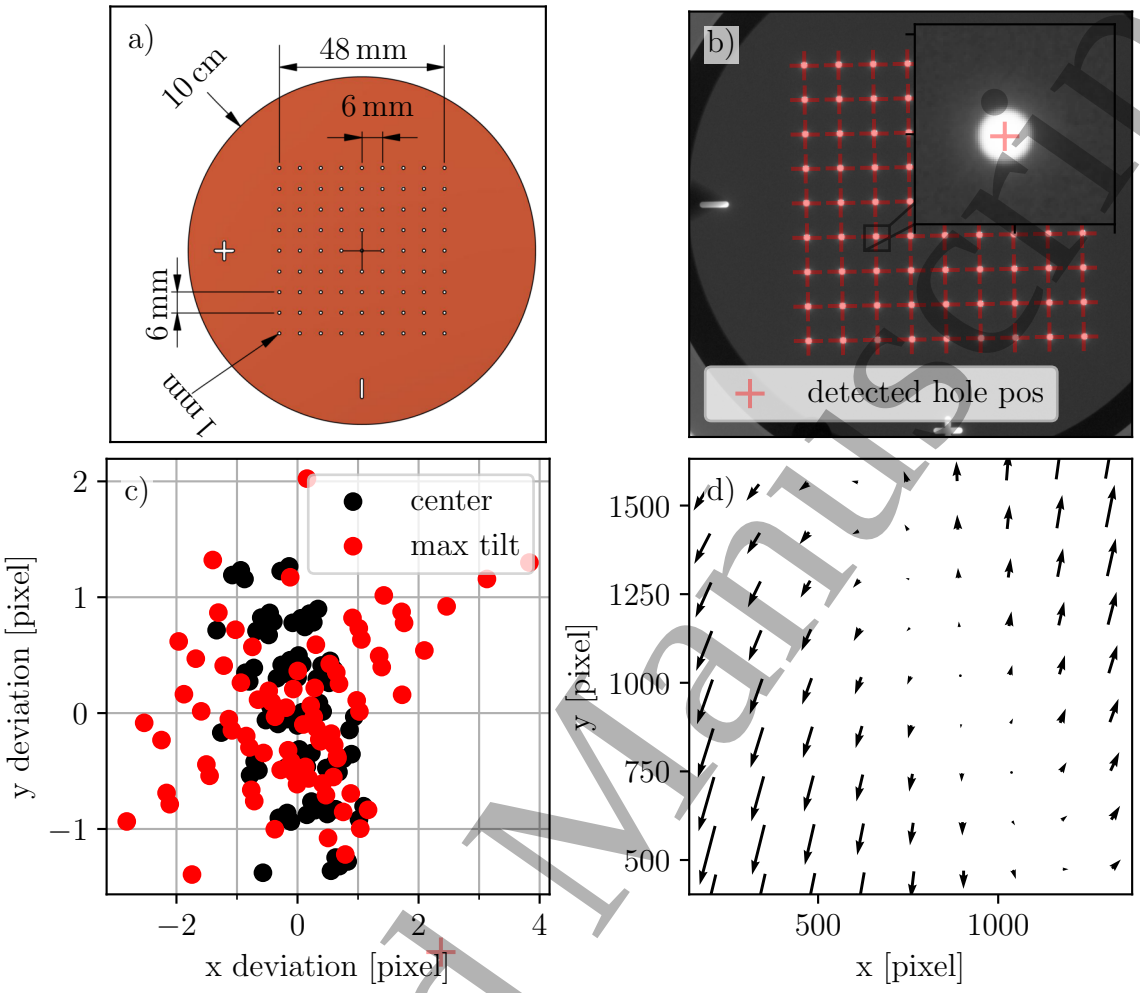

Figure 6: Projective calibration for AXT measurements. a) shows the geometry of the calibration phantom used to track the movement of grating points with rotation. b) shows a sample radiograph of the hole phantom and the center positions of the holes as determined by a peak finding algorithm. c) shows the x and y deviations of the hole positions calculated via fit from the positions determined by the peak finding algorithm for the center radiograph and an image taken at maximum tilt in θ and φ direction. The arrows in plot d) depict the change in position of the tracking holes with the rotation of the phantom. The roots of the arrows are located at the original position, the tips point towards the shifted positions, lengths are not drawn to an absolute scale.

pixels even less. This deviation is barely larger than the uncertainty of the position determination of the holes during peak finding and for typical flat panel detectors, this is also close to the resolution limit.

The fit parameters are used to calculate artificial registration points over the entire grating area for each radiograph. Subtracting the positions of these registration points of the center radiograph and any other radiograph yields a deformation vector field indicating the warping introduced by tilting. The movement of the registration points

Table 2: Overview of parameters for gratings under test. Information provided by the manufacturer, gold heights are design values.

Grating Nr.	DC	p [µm]	h [µm] resist	h [µm] gold	α_{bridge} [°]	material	Wafer thickness [µm]
9076	0.54	6.0	114	80	0	graphite	750
6779	0.5	6.0	96	75	7	graphite	1000
0882	0.53	4.8	160	80/140	0	SiTiOx	525

between two radiographs is visualized in Figure 6 d). The deformation vector field is used to map back grating points in each radiograph to a common position in the center radiograph.

3.2. Grating parameter maps

Different gratings were examined to test 2D AXT measurements and benchmark the analysis framework. For this reason, the newly acquired parameter maps are shown alongside those presented in [14], highlighting similarities and newly obtained information. An integration time of 1.6 s per AXT radiograph was chosen for all gratings. All gratings and their relevant design parameters are listed in Table 2.

9076: The first grating is a 6 µm period absorption grating manufactured on a 750 µm thick graphite wafer. The resist bridges were measured to be upright, meaning without resist bridge tilt. A φ range of ±8° is chosen and sampled with 0.125° steps, the θ direction is sampled using a step width of 0.3° over a range of ±9.15°, yielding a total of 7998 individual AXT radiographs.

The duty cycle, area duty cycle, and fill factor maps are depicted in Figure 7. They all show a gradient from the lower-left region of the grating to the upper-right. The five rectangular structures close to the left boundary of the grating are control structures placed there during manufacturing for positioning purposes. They do not contain grating bars; therefore, the fits fail. The fill factor is determined to be in the range of 94 % to 96 % over the entire grating area. This value is consistent with the value determined from a high-resolution radiograph, acquired using a Rigaku Micron LC camera with an effective pixel pitch of 0.27 µm. The radiograph is shown in Figure 7 d).

With graphite wafers, cracks tend to form within the grating structure, due to an uneven substrate surface. This effect is already visible over the entire grating area within the duty cycle maps in Figure 7 as small-scale wave-like structures. A similar but more pronounced structure can be seen in the map of the grating lamella rotation as shown in Figure 8 a). Over larger areas of the grating, mostly on the left side of the map, thin lines of alternating lamella rotation direction are visible. The 9076 grating was previously bent to better conform to the shape of the cone beam [23, 24]. The formation

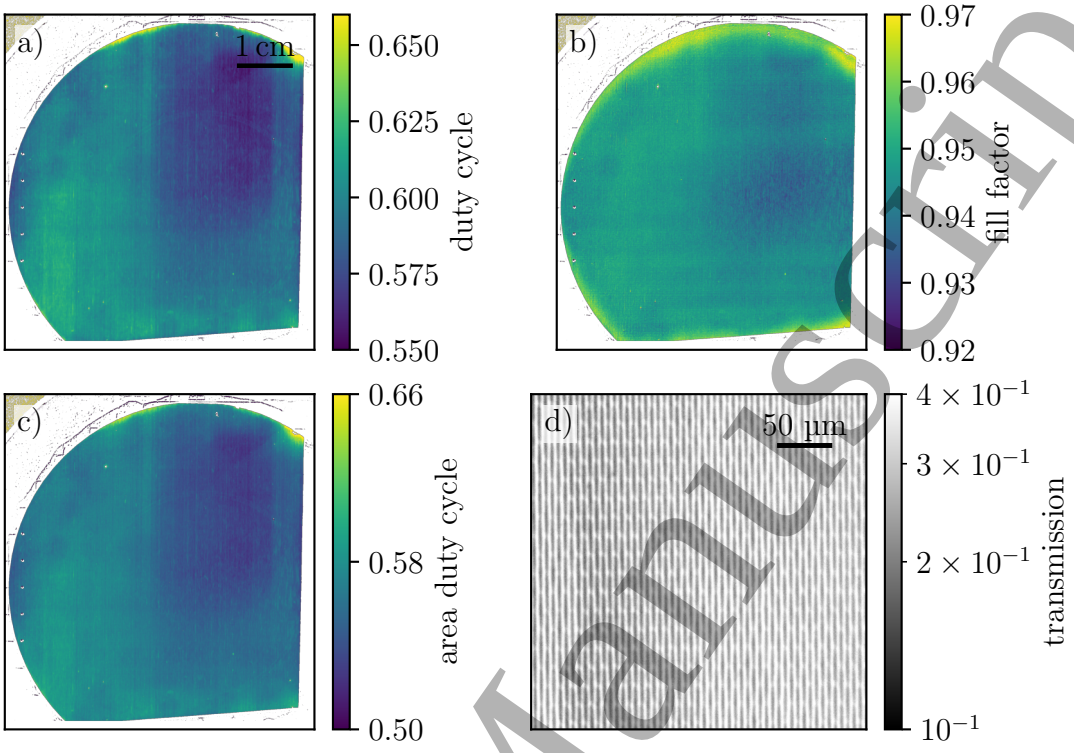

Figure 7: Duty cycle a), fill factor b) and area duty cycle c) parameter maps of the 6 µm 9076 grating. Also shown is a high-resolution radiograph of the grating bar structures in d).

of cracks is likely promoted along the vertical direction by the bending process and the grating bar alignment. The round edge of the grating surface is close to the substrate edge, where the clamp force was applied, possibly explaining why the central part of the grating does not show as many cracks. Figure 8 b)–e) show selected areas from the lamella rotation map in greater detail. As can be seen in b), localized defects are also visible in the lamella rotation map since the fits required to determine lamella rotation fail if the AXT surface is not present. c) and e) show small-scale defects that did not completely prevent the fit but are still visible within the lamella rotation map. d) shows a transition region within the lamella rotation.

6779: The second sample also has a grating period of 6 µm but is manufactured on a 1000 µm thick graphite wafer. The grating consists of two areas with different design absorber heights (80/140 µm) and uses tilted resist bridges with a design tilt of about 7°. The lower design height in one of the segments requires wider angular sampling in φ direction, so a range of ±9° is chosen. To compensate, the θ range is reduced to ±8° resulting in a total of 9425 radiographs. The starting point of the θ direction is moved to +7° to account for the tilted resist bridges. This is visible as rotated and slightly warped control structures towards the left and right grating edges. Since the new reference already contains perspective warping, all other radiographs are transformed

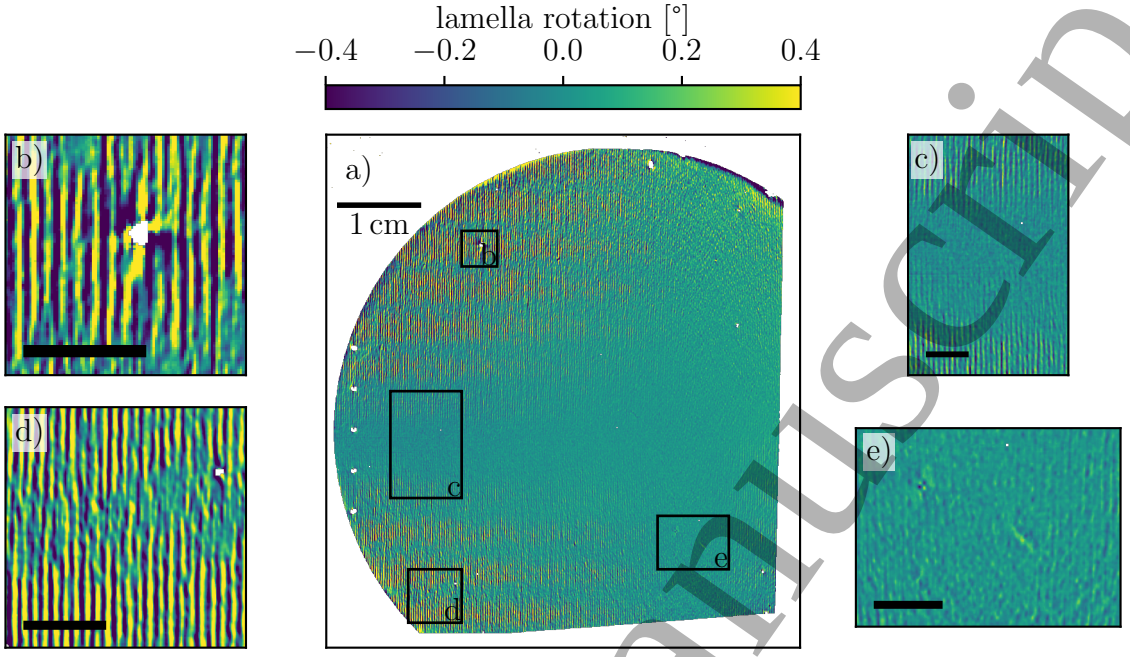

Figure 8: Lamella rotation map of the 9076 grating. a) shows the entire grating area, b)-e) show individual zoomed-in areas denoted by the rectangles in the full map. If not stated differently, the scale bars indicate a size of 2 mm.

to also include this warping.

The duty cycle map, shown in Figure 9 a), contains a downward-facing triangular structure. Otherwise, the duty cycle is similar in both segments, which is to be expected since the same mask was used during the lithography for both segments.

The height map for the 6779 grating is calculated in two steps, as the different heights mean that the local minima are located at different angular distances from the ridge and therefore require different fit regions. As a result, the split height map shown in Figure 9 b) is obtained. It clearly shows the boundary of the two regions and how the absorber heights change quickly close to this boundary. The approximate heights in each region are 65 µm and 125 µm respectively, which is about 15 µm lower than design height in both cases. Such deviations from the design height are plausible for gratings manufactured using the LIGA process, as the grating height is determined by the duration of the electroplating step. The challenges associated with thickness vs. time stem from various factors, including unsuitable electrical currents, small temperature fluctuations, and impurities in the plating solution. The resulting height deviations are usually not an issue, as long as the structure is high enough to achieve sufficient X-ray absorption for the targeted design energy.

The two areas of the grating are visible on the fill factor map (Figure 9 c)), revealing a difference of approximately 2%. This result is unexpected, as the same lithography mask was used for both segments. The discrepancy can be attributed to the relationship between X-ray absorption, photon energy and gold thickness. For the

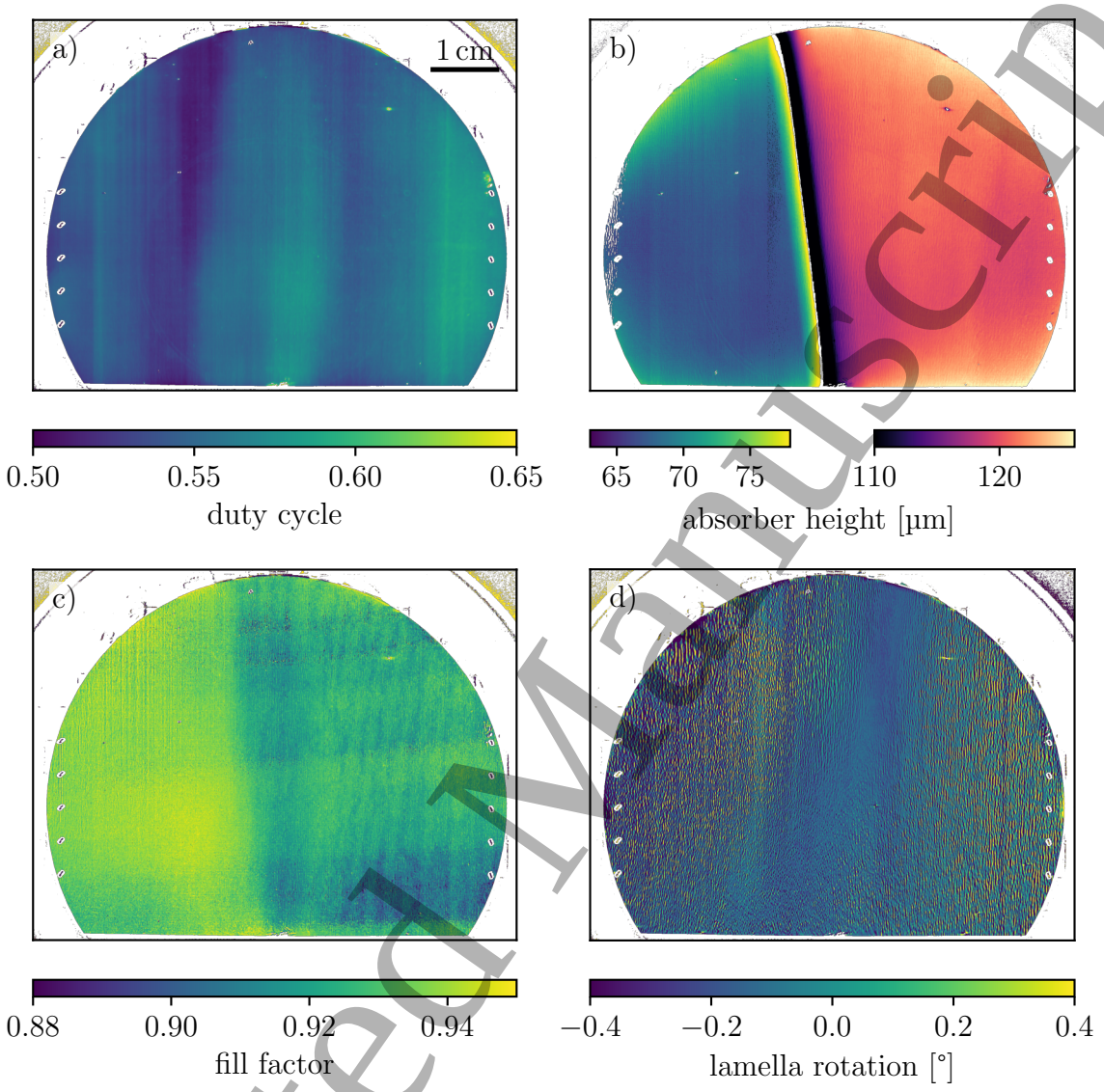

Figure 9: Parameter maps of the 6779 grating. a) shows duty cycle, b) the absorber height, c) the fill factor and d) lamella rotation. The grating area is divided into two sections with different design absorber heights.

two real thicknesses, transmission is still significant for 45 kV acceleration voltage. This effect is not as apparent in the duty cycle map because it is derived from radiographs where the θ-axis is tilted by approximately 9°. This tilt increases the effective depth of the absorbing material by up to 10 µm, thereby reducing overall transmission through the tilted bars. Lowering the acceleration voltage corrects this effect at the expense of further increasing the exposure time.

The lamella rotation map in Figure 9 d) shows vertical small-scale structures over the entire grating area. Compared to the small-scale structures in the 9076 grating, they are not as long and look more chaotic. This may stem from the thicker graphite wafer supporting the grating structure differently and the fact that the 6779 grating has

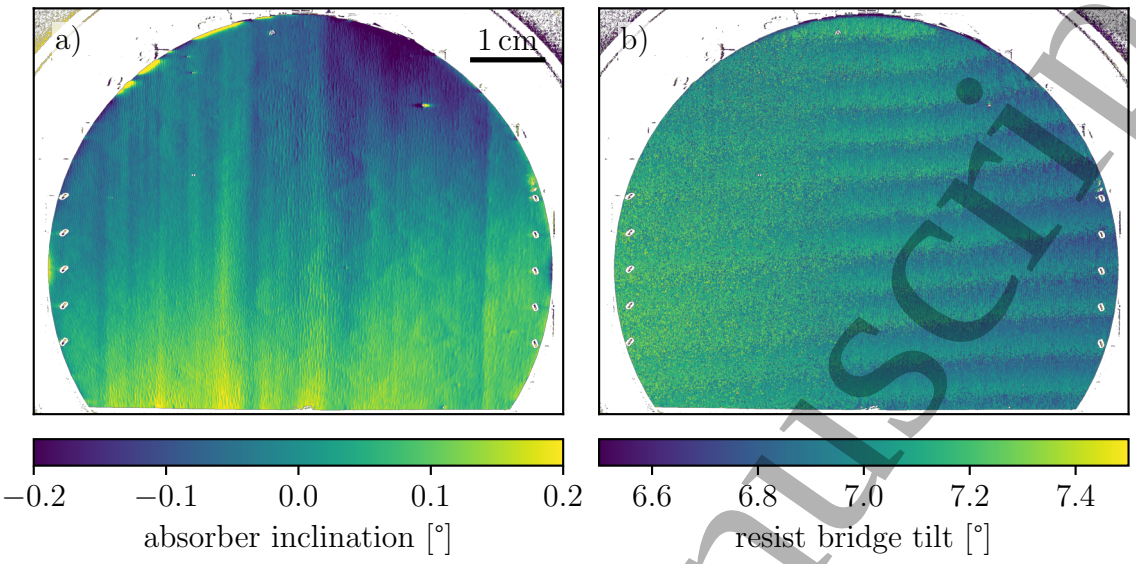

Figure 10: Additional parameter maps for the 6779 grating. a) shows the absorber inclination and b) the tilt of the resist bridges.

not yet been bent.

The absorber inclination map, depicted in Figure 10 a), shows interesting structures as well. The small-scale grating cracks are once again visible as horizontal waviness present over the entire grating area. Additionally, the right-hand side of the grating contains different, vertically wave-like structures not seen in the other parameter maps. Finally, the absorber inclination map also contains straight vertical lines, for example close to the left and right edges, that are also seen in the duty cycle map. These lines could be the result of issues with the lithography mask, for example defects in the mask or inconsistencies during mask tiling. Such issues could create large, straight gaps in the grating structure impacting multiple parameter maps.

The tilted resist bridges are best seen in Figure 10 b). Once again, the divide between the two segments is present, but both segments show a tilt of about 7°. The broader global maxima resulting from the lower absorber height in the left segment complicates the determination of the maximum position used for the resist bridge tilt calculation, thereby increasing noise in the left segment. A horizontal periodic structure, where the absorber tilt varies by approximately ±0.2° is overlaid across the entire grating area.

0882: The last grating has a 4.8 µm period and is manufactured on a 525 µm SiTiOx wafer using an inverted layout design. The lamella structure of this grating is visible in the SEM image shown in Figure 11 d). It consists of unit cells stabilized by a central resist spine, which is divided by long resist bars parallel to the grating bar direction. The grating bars are additionally interconnected by absorbing material bridges, increasing the total ratio between resist and absorbing material. This more complicated layout

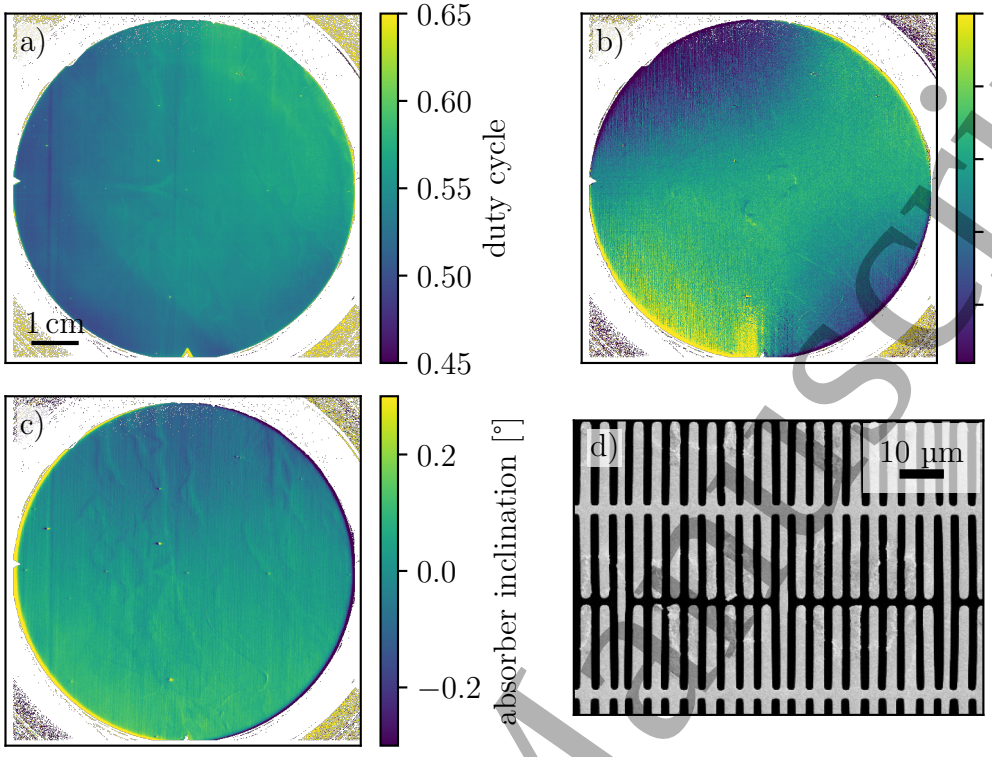

Figure 11: Parameter maps and lamella structure of the 0882 grating. a) shows the duty cycle, b) the lamella rotation and c) the absorber inclination. d) depicts an electron microscopy image of the lamella structure over several unit cells. The dark regions are the lower gold absorbing parts of the grating, while the brighter parts show the stabilizing resist.

prevents Equation 11 from being used for fill factor calculation.

The smaller period means that the first minimum in φ direction is reached for smaller tilt angles (Equation 9), so a range of $\pm 7.5°$ in φ direction with finer sampling of $0.08125°$ is chosen. The global peak of the AXT surface is broader than for the previously examined gratings, most likely due to the higher ratio of non-absorbing resist material in the grating structure. To ensure the collection of useful data beyond the central peak, the sampling range in θ direction is increased to $\pm 9°$ and the sampling distance is increased to $0.25°$, resulting in a total number of 14769 AXT radiographs.

A collection of result maps from these measurements is presented in Figure 11. The triangular structures seen on all parameter maps on the left and bottom edge are parts of the mounting system. All maps once again reveal the smaller-scale, localized, dot-like defects distributed across the grating area.

The duty cycle (Figure 11 a)) seems to be split into two distinct regions, clearly separated by a sharp line. A smaller region towards the bottom left edge, and a larger region with duty cycles between 55 % and 60 % over the rest of the grating.

The lamella rotation map in Figure 11 b) reveals several interesting features. A gradient of lamella rotation connects the lower-left and upper-right corners, while the

remaining quadrants show lamellae pointing in the opposite direction. In the lower-right corner, multiple long lines are visible. Additionally, two semicircular structures can be seen at the center of the grating. None of these structures appear in the other maps, highlighting the complementary nature of the information conveyed by each map.

The absorber inclination map in Figure 11 c) exhibits fewer small-scale ripples compared to the other gratings. Instead, larger-scale, vertical, wave-like cracks are visible, primarily near the center of the grating. A reason for the difference could be the layout or the silicon wafer, owing to its smoother surface.

4. Conclusion

Measuring X-ray transmission through grating structures under the effect of two-dimensional rotation rather than one-dimensional rotation, provides new information. The lamella rotation map reveals local shifts and cracks in the grating structure. Together with the fill factor and area duty cycle maps, tools for assessing the quality of auxiliary resist bridges are now available. Additionally, a new method for correcting distortions arising from the movement of the gratings during measurements has been introduced. The high quality of this correction has been demonstrated, further enhancing the spatial resolution in all result maps.

Bidirectional angular X-ray transmission measurements could serve both as a quality control tool—particularly valuable in grating production—and as a means of improving grating production. For example, large-scale parameter maps could be generated to assess variations in manufacturing processes while refining manufacturing methods or simply as a final, nondestructive quality control step in grating production. The longest total integration time for a single grating in this study was approximately 7 hours, but there are several opportunities for optimization. For instance, utilizing a detector with a larger pixel pitch increases the number of photons captured per pixel, leading to a reduction in integration times while maintaining the same signal-to-noise ratio. Choosing a pixel pitch of 100 µm, only doubling the pixel pitch compared to the data presented in this study, would still result in sufficient resolution for most gratings while cutting down integration time by a factor of four. Additionally, transitioning to setups with larger source-grating distances could mitigate the effects of the cone beam source, thereby reducing the angular range that needs to be sampled for a complete AXT surface at each grating point. The total number of sampling points could also be reduced by increasing the sampling point distance or using non-uniform sampling. The potential reduction of sampling points depends on grating parameters, as they determine the shape of the AXT surface. Similarly, the integration time per projection could be reduced. The least prominent feature of the AXT surface are the local minima, meaning that the first parameter retrieval to fail when integration time is reduced, is typically the absorber height.

While only standard-layout and inverted-layout gratings (manufactured using deep X-ray lithography, though they could also be fabricated using other techniques such as

deep reactive ion etching) were examined in this manuscript, bidirectional angular X-ray measurements also show promise for more advanced grating geometries and alternative materials. In general, different geometries may require adapting the grating parameter retrieval procedure or may render some parameters inaccessible. For example, with slight modifications to the parameter retrieval process, grating geometries designed for fan-beam sources [25, 26] could be characterized in regard to their conformance to the targeted fan-beam geometry and simultaneously compared in quality with conventional gratings.

Acknowledgments

The authors acknowledge the support of the Karlsruhe Nano Micro Facility (KNMF), a Helmholtz Research Infrastructure at Karlsruhe Institute of Technology, and microworks GmbH for fabricating some of the gratings used in this publication.

References

[1] Pfeiffer F, Herzen J, Willner M, Chabior M, Auweter S, Reiser M and Bamberg F 2013 *Zeitschrift für Medizinische Physik* **23** 176–185 ISSN 0939-3889 schwerpunkt: Röntgenbasierte Phasenkontrast Bildgebung URL https://www.sciencedirect.com/science/article/pii/S0939388913000263

[2] Michel T, Rieger J, Anton G, Bayer F, Beckmann M W, Durst J, Fasching P A, Haas W, Hartmann A, Pelzer G, Radicke M, Rauh C, Ritter A, Sievers P, Schulz-Wendtland R, Uder M, Wachter D L, Weber T, Wenkel E and Zang A 2013 *Physics in Medicine & Biology* **58** 2713 URL https://dx.doi.org/10.1088/0031-9155/58/8/2713

[3] Ludwig V, Seifert M, Niepold T, Pelzer G, Rieger J, Ziegler J, Michel T and Anton G 2018 *Journal of Imaging* **4** ISSN 2313-433X URL https://www.mdpi.com/2313-433X/4/4/58

[4] Wegert L, Schreiner S, Rauch C, Albertazzi B, Bleuel P, Fröjdh E, Koenig M, Ludwig V, Martynenko A S, Meyer P, Mozzanica A, Müller M, Neumayer P, Schneider M, Triantafyllidis A, Zielbauer B, Anton G, Michel T and Funk S 2024 *Matter and Radiation at Extremes* **9** 047803 ISSN 2468-2047 URL https://doi.org/10.1063/5.0200440

[5] Pfeiffer F, Weitkamp T, Bunk O and David C 2006 *Nature physics* **2** 258–261

[6] Chantler C T 1995 *Journal of Physical and Chemical Reference Data* **24** 71–643 ISSN 0047-2689 URL https://doi.org/10.1063/1.555974

[7] Murakami H, Katsuki A, Sajima T, Uchiyama K, Yoshida I, Hamano Y and Honda H 2020 *Measurement Science and Technology* **31** 075902 URL https://dx.doi.org/10.1088/1361-6501/ab7efc

[8] Murakami H, Murakami H, Katsuki A, Sajima T and Uchiyama K 2023 *Precision Engineering* **80** 72–81 ISSN 0141-6359 URL https://www.sciencedirect.com/science/article/pii/S0141635922002525

[9] Soman S, Pereira S F and Gawhary O E 2022 *Journal of Optics* **24** 034006 URL https://dx.doi.org/10.1088/2040-8986/ac4abb

[10] Soman S, Horsten R C, Scholte T and Pereira S F 2024 *Measurement Science and Technology* **35** 075905 URL https://dx.doi.org/10.1088/1361-6501/ad3b2a

[11] Yang T, Chen X, Liu S, Zhang J and Liu S 2023 *Measurement Science and Technology* **34** 125001 URL https://dx.doi.org/10.1088/1361-6501/acec8d

[12] Mattila A, Nysten J, Heikkinen V, Kilpi J, Korpelainen V, Hansen P E, Karvinen P, Kuittinen

M and Lassila A 2024 *Measurement Science and Technology* **35** 085025 URL https://dx.doi.org/10.1088/1361-6501/ad4e52

[13] Crosby K, Eberle A L and Zeidler D 2016 *MRS Advances* **1** 1915–1920

[14] Gustschin N, Gustschin A, Meyer P, Viermetz M, Riederer P, Herzen J, Mohr J and Pfeiffer F 2019 *Opt. Express* **27** 15943–15955 URL https://opg.optica.org/oe/abstract.cfm?URI=oe-27-11-15943

[15] Jefimovs K, Romano L, Vila-Comamala J, Kagias M, Wang Z, Wang L, Dais C, Solak H and Stampanoni M 2017 High-aspect ratio silicon structures by displacement talbot lithography and bosch etching *Advances in Patterning Materials and Processes XXXIV* vol 10146 (SPIE) pp 140–146

[16] Romano L and Stampanoni M 2020 *Micromachines* **11** ISSN 2072-666X URL https://www.mdpi.com/2072-666X/11/6/589

[17] Meyer P, Schulz J and Saile V 2010 *Micromanufacturing Engineering and Technology* 365–391

[18] Becker E, Ehrfeld W, Hagmann P, Maner A and Münchmeyer D 1986 *Microelectronic engineering* **4** 35–56

[19] Shi Z, Jefimovs K, Romano L and Stampanoni M 2020 *Micromachines* **11** ISSN 2072-666X URL https://www.mdpi.com/2072-666X/11/9/864

[20] Shi Z, Jefimovs K, La Magna A, Stampanoni M and Romano L 2022 *Applied Surface Science* **588** 152938 ISSN 0169-4332 URL https://www.sciencedirect.com/science/article/pii/S0169433222005104

[21] Pinzek S, Beckenbach T, Viermetz M, Meyer P, Gustschin A, Andrejewski J, Gustschin N, Herzen J, Schulz J and Pfeiffer F 2021 *Journal of Micro/Nanopatterning, Materials, and Metrology* **20** 043801 URL https://doi.org/10.1117/1.JMM.20.4.043801

[22] Schüttler M, Meyer P, Schaff F, Yaroshenko A, Kunka D, Besser H, Pfeiffer F and Mohr J 2016 *Measurement Science and Technology* **27** 025015 URL https://dx.doi.org/10.1088/0957-0233/27/2/025015

[23] Revol V, Kottler C, Kaufmann R, Jerjen I, Lüthi T, Cardot F, Niedermann P, Straumann U, Sennhauser U and Urban C 2011 *Nuclear Instruments and Methods in Physics Research Section A: Accelerators, Spectrometers, Detectors and Associated Equipment* **648** S302–S305

[24] Richter M, Beckenbach T, Daerr H, Prevrhal S, Börner M, Gutekunst J, Zangi P, Last A, Korvink J G and Meyer P 2022 *Journal of Micro/Nanopatterning, Materials, and Metrology* **21** 024901 URL https://doi.org/10.1117/1.JMM.21.2.024901

[25] Shi Z, Jefimovs K, Romano L, Vila-Comamala J and Stampanoni M 2021 *Opt. Lett.* **46** 3693–3696 URL https://opg.optica.org/ol/abstract.cfm?URI=ol-46-15-3693

[26] Josell D, Raciti D, Gnaupel-Herold T, Moffat T P, Romano L, Rawlik M, Chen L, Yu Q, Stampanoni M, Pereira A and Stauber M 2024 *ECS Meeting Abstracts* **MA2024-02** 1924 URL https://dx.doi.org/10.1149/MA2024-02221924mtgabs